

QLingNet: An efficient and flexible modeling framework for subsonic airfoils

Kuijun Zuo^a, Zhengyin Ye^a, Linyang Zhu^b, Xianxu Yuan^{b,*}, Weiwei Zhang^{a,*}

^a*School of Aeronautics, Northwestern Polytechnical University, Xi'an, 710072, China*

^b*State Key Laboratory of Aerodynamics, China Aerodynamics Research and Development Center, Mian'yang, 621000, China*

Abstract

Artificial intelligence techniques are considered an effective means to accelerate flow field simulations. However, current deep learning methods struggle to achieve generalization to flow field resolutions while ensuring computational efficiency. This paper presents a deep learning approach for rapid prediction of two types of subsonic flow fields with different resolutions. Unlike convolutional neural networks, the constructed feature extractor integrates features of different spatial scales along the channel dimension, reducing the sensitivity of the deep learning model to resolution while improving computational efficiency. Additionally, to ensure consistency between the input and output resolutions of the deep learning model, a memory pooling strategy is proposed, which ensures accurate reconstruction of flow fields at any resolution. By conducting extensive qualitative and quantitative analyses on a given test dataset, it is demonstrated that the proposed deep learning model can achieve a three-order-of-magnitude speedup compared to CPU-based solvers while adapting to flow fields of arbitrary resolutions. Moreover, the prediction accuracy for pressure exceeds 99%, laying the foundation for the development of large-scale models in the field of aerodynamics.

Keywords: Deep learning, Computational fluid dynamics, Flow field prediction, Machine learning

1. Introduction

In the engineering applications of computational fluid dynamics (CFD) [1, 2], the Reynolds-Averaged Navier-Stokes (RANS) method is widely employed for solving flow

*Corresponding author

Email addresses: yuanxianxu2023@163.com (Xianxu Yuan), aeroelastic@nwpu.edu.cn (Weiwei Zhang)

fields [3] and analyzing the aerodynamic performance of airfoils [4–6]. However, as the complexity of engineering problems increases, solving the Navier-Stokes (NS) equations becomes time-consuming and requires significant memory resources [7]. Especially in the aerodynamic optimization design of aircraft [8, 9], modifying a certain parameter often necessitates repetitive tasks such as grid partitioning and solving the NS equations. The flourishing development of artificial intelligence technology [10–13] has provided a new perspective for the rapid solution of flow fields.

As a pioneering effort, Guo et al. [14] utilized convolutional neural networks (CNNs) to predict steady-state laminar velocity fields in both two and three dimensions. Through experiments, they found that CNNs could achieve computational speeds approximately four orders of magnitude faster than CPU-based solvers and two orders of magnitude faster than GPU-based solvers. Wu and his team [15] took the signed distance field (SDF) and flow field boundary conditions as inputs to a neural network. They employed CNN to predict the velocity and pressure fields of the NACA0012 airfoil series under incompressible steady-flow conditions. Experimental results indicated that using neural networks could achieve a threefold increase in speed compared to traditional CFD simulation methods, with a prediction error of less than 1%. As mentioned above, CNNs have been widely applied in the rapid simulation of airfoil flow fields. Similar works include the DeepCFD network architecture proposed by Mateus et al. [16], the Mesh-Conv proposed by Hu et al. [17], and the CNNFOIL model for rapid simulation of transonic airfoil flow fields introduced by Cihat [18, 19], among others. In addition to CNNs, fully connected neural networks (FNNs) [8, 20, 21], generative adversarial networks (GANs) [22–24], graph neural networks (GNNs) [25–27], point clouds [28, 29], and Transformer neural network architectures [30–33] have also been extensively employed in the rapid simulation and solution tasks of flow fields. However, a survey of existing literature reveals challenges in achieving predictions for flow fields at different resolutions. The main challenges include: (1) Current neural network models lack effective methods for handling multi-scale flow field structures. (2) If we consider the flow field prediction task as a field-to-field modeling problem similar to a black-box model, ensuring adaptive handling of flow field resolution during both model training and inference stages is essential. It is also crucial to maintain consistency between the predicted output resolution of the neural network model and the input resolution. (3) While multi-layer perceptrons (MLP) can generalize across different

grid resolutions, the training cost and memory overhead of the model exhibit a quadratic relationship with the input resolution of the airfoil grid. Inspired by the work of Chen et al. [34], we propose the QLingNet (see 5 for an explanation of the name), a deep learning flow field rapid prediction network architecture designed for multi-scale subsonic airfoil flow field structures. The primary contributions of this study can be summarized as follows:

- Proposed a computationally efficient and flexible deep learning model for the rapid prediction of subsonic variable-topology airfoil flow fields.
- Generated two types of subsonic airfoil flow fields with distinct topological structures, namely the University of Illinois Urbana-Champaign (UIUC) [35] airfoil flow field database and the class function/shape function transformation (CST) [36] airfoil parameterized perturbation airfoil flow field database.
- Utilizing the QLingNet ensures linear computational complexity for calculating flow fields at different resolutions.
- Integrated a memory pool module into the QLingNet, ensuring that the neural network’s output flow field size remains consistent with the input flow field size.

The rest of this paper is organized as follows. Section II mainly describes the physical governing equations used for flow field simulation and the QLingNet network framework. Section III primarily discusses the two types of airfoil flow field datasets with different geometries and resolutions. Section IV shows and discusses the results of the QLingNet neural network model training and test. And the conclusion is given in Section V.

2. Methodology

2.1. Physical equations

The training data for the neural network model used here is obtained through simulation calculations conducted by the Platform for Hybrid Engineering Simulation of Flows (PHengLEI) [37] software developed by the China Aerodynamics Research and Development Center (CARD C). Specifically, the PHengLEI computation program obtains the physical information at each discrete point in the flow field by solving the RANS equations on the structural grid of a two-dimensional airfoil.

The airfoil is simulated under the following conditions: Mach number (Ma) = 0.5, angle of attack (AOA) = 3.86 °, and Reynolds number (Re) = 3×10^6 . Below is a brief introduction to the governing equations and the SA (Spalart-Allmaras) turbulence model employed in the simulation software calculations. The RANS equations under Favre averaging are:

$$\frac{\partial \bar{\rho}}{\partial t} + \frac{\partial}{\partial x_j} (\bar{\rho} \bar{u}_j) = 0 \quad (1)$$

$$\frac{\partial}{\partial t} (\bar{\rho} \tilde{u}_i) + \frac{\partial}{\partial x_j} (\bar{\rho} \tilde{u}_i \tilde{u}_j) = -\frac{\partial \bar{p}}{\partial x_i} + \frac{\partial \bar{\tau}_{ij}}{\partial x_j} - \frac{\partial}{\partial x_j} \overline{\rho u_i'' u_j''} \quad (2)$$

$$\frac{\partial}{\partial t} (\bar{\rho} \tilde{e}) + \frac{\partial}{\partial x_j} (\bar{\rho} \tilde{u}_j \tilde{e}) = \frac{\partial}{\partial x_j} \left(\kappa \frac{\partial \bar{T}}{\partial x_j} \right) - \bar{p} \frac{\partial \tilde{u}_j}{\partial x_j} + \bar{\Phi} - \overline{u_j'' \frac{\partial p'}{\partial x_j}} - \frac{\partial}{\partial x_j} \overline{\rho e'' u_j''} \quad (3)$$

In above equations, t represents time, p and ρ denote pressure and density, u_i and u_j represent the velocity components in the x_i and x_j directions, respectively. τ_{ij} represents the viscous stress tensor. The symbol " \sim " denotes the Favre-averaged physical quantity, a prime superscript indicates the time-averaged fluctuating momentum, and a double prime superscript signifies the fluctuating momentum under Favre averaging. $\bar{\tau}_{ij}$ represents the mean viscous stress, $\overline{\rho u_i'' u_j''}$ represents the Reynolds stress, $\bar{\Phi}$ denotes the mean flow viscous dissipation rate, the work done by fluctuating pressure along fluctuating displacement is represented by $\overline{u_j'' \frac{\partial p'}{\partial x_j}}$, and the correlation between fluctuating energy and fluctuating velocity is denoted by $\overline{\rho e'' u_j''}$.

Here, the SA turbulence model is employed to close the RANS equations. Turbulent eddy viscosity is defined as:

$$\mu_t = \rho \hat{\nu} f_{v1} \quad (4)$$

$$f_{v1} = \frac{\chi^3}{\chi^3 + C_{v1}^3}, \chi = \frac{\hat{\nu}}{\nu} \quad (5)$$

In Eq. 5, C_{v1} is a model parameter typically set to 7.1, ν is the kinematic molecular viscosity. Further deriving the transport equation:

$$\begin{aligned} \frac{\partial \hat{v}}{\partial t} + u_j \frac{\partial \hat{v}}{\partial x_j} = & C_{b1}(1 - f_{t2})\hat{S}\hat{v} - \left(C_{w1}f_w - \frac{C_{b1}}{\kappa^2}f_{t2} \right) \left(\frac{\hat{v}}{d'} \right)^2 \\ & + \frac{1}{\sigma} \left\{ \frac{\partial}{\partial x_j} \left[(v + \hat{v}) \frac{\partial \hat{v}}{\partial x_j} \right] + C_{b2} \frac{\partial \hat{v}}{\partial x_i} \cdot \frac{\partial \hat{v}}{\partial x_i} \right\} \end{aligned} \quad (6)$$

$$\hat{S} = S + \frac{\hat{v}}{\kappa^2 d^2} f_{v2} \quad (7)$$

$$f_{v2} = 1 - \frac{\chi}{1 + \chi f_{v1}}, f_{t2} = C_{t3} \exp(-C_{t4} \chi^2), f_w = g \left(\frac{1 + C_{w3}^6}{g^6 + C_{w3}^6} \right)^{1/6} \quad (8)$$

$$g = r + C_{w2}(r^6 - r), r = \frac{\hat{v}}{\hat{S} \kappa^2 d^2}, C_{w1} = \frac{C_{b1}}{\kappa^2} + \frac{1 + C_{b2}}{\sigma} \quad (9)$$

In Eq. 6, 7, 8, 9, \bar{v} is the state variable of the SA turbulence model, d is the wall distance, S represents the magnitude of the vorticity. C_{b1} , C_{b2} , σ , C_{w1} , C_{w2} , C_{w3} , C_{v1} , κ , C_{t3} and C_{t4} represent model parameters. In accordance with the empirical findings outlined in reference [37], the model parameters are conventionally set to $C_{b1} = 0.1355$, $C_{b2} = 0.622$, $\sigma = \frac{2}{3}$, $\kappa = 0.41$, $C_{w2} = 0.3$, $C_{w3} = 2$.

2.2. Cycle fully-connected module

First, we represent the flow field feature maps input to the neural network as $X \in \mathbb{R}^{H \times W \times C_{in}}$, where H , W , and C_{in} represent the height, width, and number of channels of the grid, respectively. As shown in Figure 1(a), for convolutional neural networks, the main approach is to extract flow field features by sliding fixed convolutional kernels over the given feature maps. The calculation formula is as follows:

$$\begin{cases} H_{out} = \frac{H_{in} + 2 \times P_0 - K_0}{S_0} + 1, \\ W_{out} = \frac{W_{in} + 2 \times P_1 - K_1}{S_1} + 1. \end{cases} \quad (10)$$

In the above formula, P_i represents the padding size, K_i represents the size of the convolutional kernel, and S_i represents the stride of the convolutional kernel. However, the above-mentioned spatial convolutional neural network architectures struggle to flexibly handle flow fields with different resolutions. The channel fully connected (channel FC) model shown in Figure 1(b) extracts flow field features along the channel dimension at fixed positions (i, j) . Although it can flexibly handle flow fields with different resolutions,

but it lacks the capability to capture contextual information of the flow field.

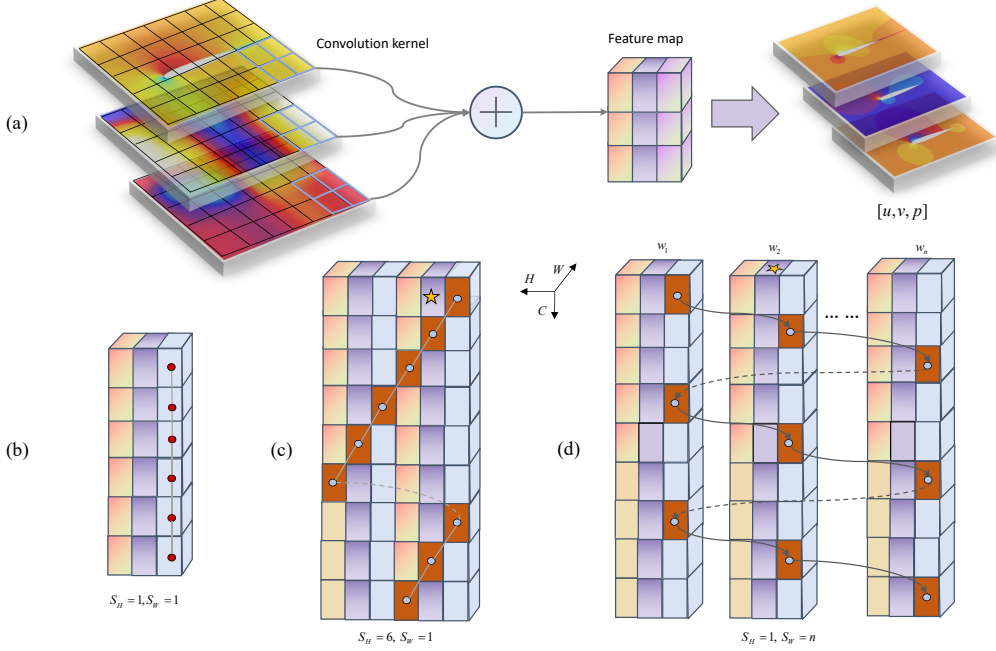


Figure 1: Comparison of CNN and CycleFC feature extraction methods.

As shown in Figure 1(c) and Figure 1(d), Cycle fully-connected (Cycle FC) introduces the $stepsizc(S_H, S_W)$ on the basis of the channel FC model to increase the model's receptive field. Its calculation formula is as follows:

$$\text{CycleFC}(\mathbf{X})_{i,j,:} = \sum_{c=0}^{C_{in}} \mathbf{X}_{i+\delta_i(c),j+\delta_j(c),c} \cdot \mathbf{W}_{c,:}^{\text{mlp}} + \mathbf{b} \quad (11)$$

In Eq. (11), $\mathbf{W}^{\text{mlp}} \in \mathbb{R}^{C_{in} \times C_{out}}$ and $\mathbf{b} \in \mathbb{R}^{C_{out}}$ are the model parameters to be optimized. $\delta_i(c)$ and $\delta_j(c)$ represent the offsets along the channels c in the S_H and S_W directions, respectively, and they are defined as:

$$\delta_i(c) = (c \bmod S_H) - 1, \delta_j(c) = (\lfloor \frac{c}{S_H} \rfloor \bmod S_W) - 1 \quad (12)$$

For Figure 1(c), when $S_H = 6, S_W = 1$, with the pentagram in the figure as the reference coordinate, when $c = \{0, 1, 2, \dots, 5\}$, the offset in the S_H direction is $\delta_i(c) = \{-1, 0, 1, 2, 3, 4\}$. In Figure 1(d), when $S_H = 1$ and $S_W = n$, $\delta_j(c) = \{-1, 0, 1, \dots, (n-2)\}$. The derivation above reveals that the Cycle FC module incorporates offset terms along the channel dimension, allowing it to retain the efficient computational capabilities while also

integrating contextual information from different spatial points. Moreover, this network architecture can generalize well to flow fields of different resolutions.

2.3. QLingNet architecture

Based on the Cycle FC component described in Section 2.2, we construct the QLingNet. Below, we provide an introduction to the fundamental modules involved in Figure 2.

Input: The flow field data for the QLingNet comprises two types. The first type consists of flow field data obtained through PHengLEI computations based on the UIUC airfoil, with a resolution of 55×403 . The second type is derived from the NACA0012 airfoil using the CST parameterization method, resulting in a flow field resolution of 120×364 . Both types of flow fields have 13 channels ($x, y, x_0, y_0, \xi, \eta, SDF, M_x, M_y, \frac{\partial x}{\partial \xi}, \frac{\partial x}{\partial \eta}, \frac{\partial y}{\partial \xi}, \frac{\partial y}{\partial \eta}$). The interpretation of the above parameters can be found in Section 3. Therefore, the flow field resolutions inputted into QLingNet are $55 \times 403 \times 13$ and $120 \times 364 \times 13$, respectively.

Patch Embedding: This module segments the flow field data inputted into QLingNet into a series of patches. Specifically, it mainly uses a two-dimensional convolutional module to accomplish the segmentation task, with hyperparameters convolutional kernel=7, stride=4, padding=2. Furthermore, it maps the channels to a higher dimension through linear mapping. Therefore, the dimension of the input features after passing through patch embedding module is $\frac{H}{4} \times \frac{W}{4} \times 64$.

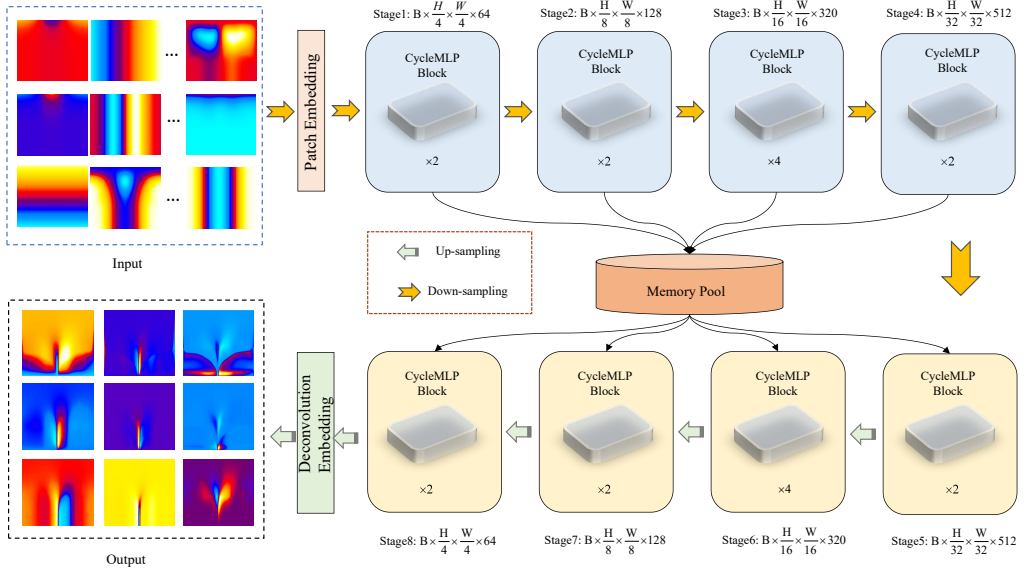


Figure 2: QLingNet neural network architecture.

CycleMLP Block: The main body of QLingNet consists of a series of CycleMLP

blocks, where multiple CycleMLP blocks extract spatial features of the flow field at different scales in a pyramid structure and perform information fusion. The detailed network structure of the CycleMLP module is illustrated in Figure 3. The spatial mapping is performed by three parallel CycleFC modules, each with different *stepsize* (1×13 , 1×1 , 13×1). The information extracted by these three CycleFC modules is further fused using an attention layer. Channel mapping is achieved through two linear layers followed by the GeLU activation function. LayerNorm and residual network layers are added before and after both the spatial and channel mappings, respectively.

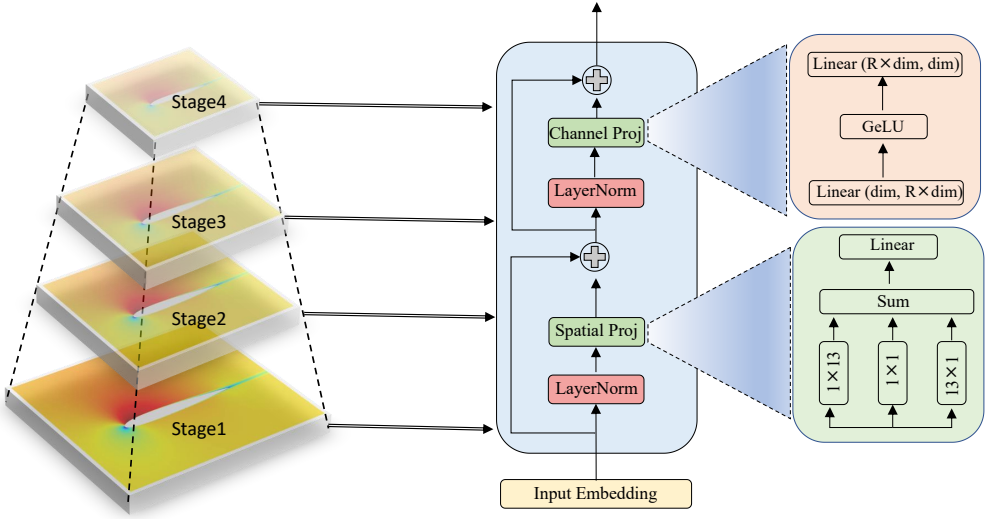


Figure 3: Feature pyramid and CycleMLP block.

Stage: Each stage consists of multiple CycleMLP blocks stacked together. In QLingNet, both the encoding and decoding layers are composed of 4 stages. The feature map resolution processed within the same stage is consistent. After each stage, there is a down-sampling layer, which reduces the spatial dimensions of the feature maps while increasing the number of channels. This ensures a reduction in computational complexity while operating in a high-dimensional feature space.

Memory pool: To ensure that QLingNet can adapt to flow fields of different resolutions, a memory pool is designed to store the feature map resolutions at each stage of the encoding down-sampling phase. During the decoding up-sampling phase, the model sequentially retrieves the corresponding feature resolutions from the memory pool, ensuring that the final output resolution of the flow field matches the original resolution. Here, the output channel number is 9 ($u, v, p, \frac{\partial u}{\partial \xi}, \frac{\partial u}{\partial \eta}, \frac{\partial v}{\partial \xi}, \frac{\partial v}{\partial \eta}, \frac{\partial p}{\partial \xi}, \frac{\partial p}{\partial \eta}$), representing the velocity

field, pressure field, and their corresponding gradient information in the computational coordinates.

Deconvolution Embedding: To restore the feature map resolution of the embedded patches back to the original flow field size, a deconvolution embedding layer is added to the final layer of the model. After passing through this layer, the output size of the flow field feature map becomes $H \times W \times 9$.

3. Data preparation

Figure 4 presents two types of flow field data with different topological structures, and they are utilized to test the generalization capability of QLingNet when facing flow fields with different resolutions. As shown in Figure 4(a), the first type of test case involves 500 airfoil geometries generated by perturbing the NACA0012 airfoil using the CST parameterization method. The grid is partitioned using an O-type mesh, as shown in Figure 4(c), with a grid size of 120×364 , where the grid height is 120 and the number of grid points per layer is 364. As depicted in Figure 4(b), the second type of test case consists of 270 airfoil geometries with significant variations from the UIUC public airfoil database. The grid is primarily partitioned using a C-type mesh, as shown in Figure 4(d), with a grid size of 55×403 . To facilitate subsequent data analysis, the first dataset will be named 'NACA0012-CST' and the second dataset will be named 'UIUC'. Using the PHengLEI solver to obtain training data for the neural network, the operating conditions are $Re=3 \times 10^6$, $AOA=3.86^\circ$, and $Ma=0.5$. 80% of the aforementioned flow field data is utilized for training the QLingNet model, 10% is allocated for cross-validation, and the remaining 10% is designated for testing.

The mapping function for the QLingNet neural network, as a type of end-to-end black-box model, can be represented as follows:

$$f(x, y, x_0, y_0, \xi, \eta, SDF, M_x, M_y, \frac{\partial x}{\partial \xi}, \frac{\partial x}{\partial \eta}, \frac{\partial y}{\partial \xi}, \frac{\partial y}{\partial \eta}) = (u, v, p, \frac{\partial u}{\partial \xi}, \frac{\partial u}{\partial \eta}, \frac{\partial v}{\partial \xi}, \frac{\partial v}{\partial \eta}, \frac{\partial p}{\partial \xi}, \frac{\partial p}{\partial \eta}) \quad (13)$$

On the left side of Eq. (13) are the thirteen features input to the neural network, while on the right side are the nine flow field variables to be predicted. As shown in Figure 5, in order to facilitate the subsequent training of the QLingNet model, following the processing strategy in reference [38], the flow field data is transformed from Cartesian coordinates

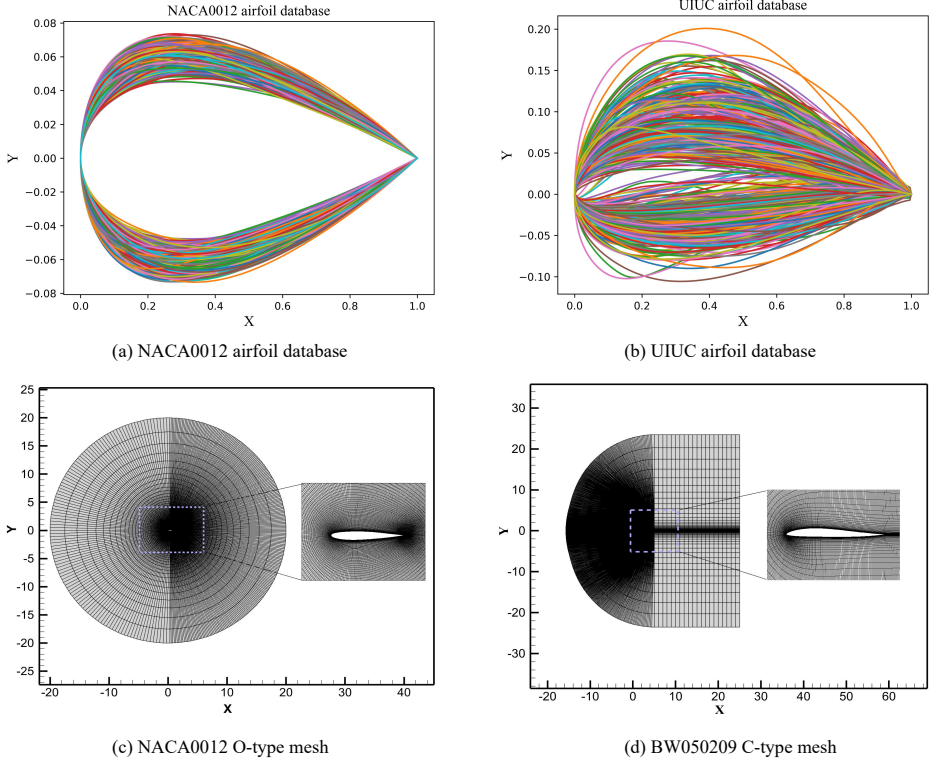


Figure 4: Two types of grids with different topological structures and airfoil database.

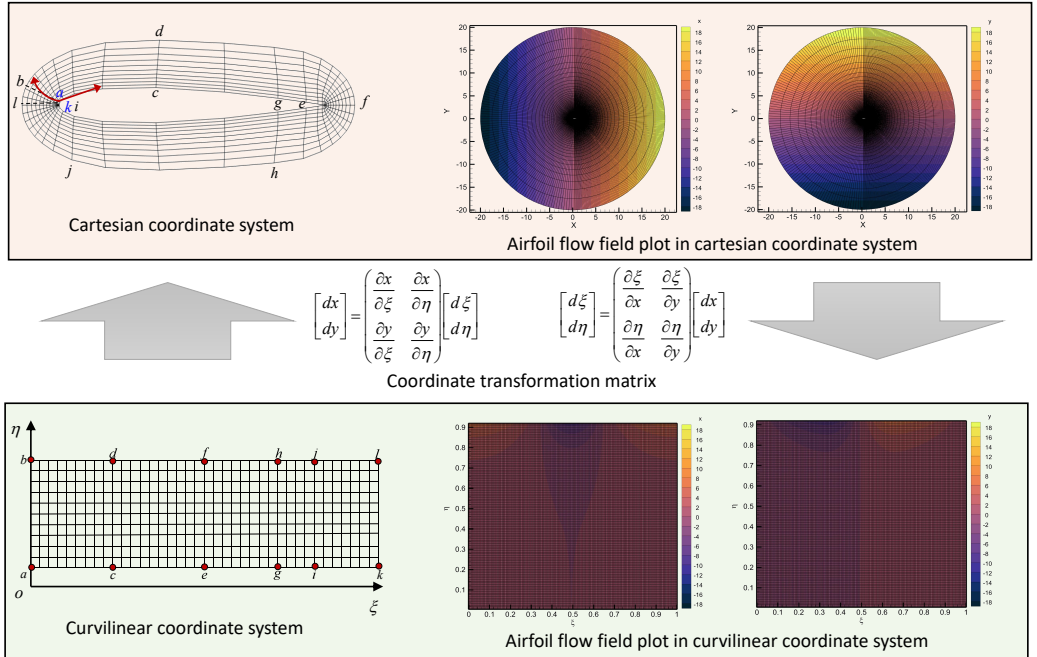


Figure 5: Conversion between curvilinear coordinates and Cartesian coordinates.

(x, y) to curvilinear coordinates (ξ, η) . x_0 and y_0 are the coordinates of the first layer of grid points on the surface. ξ and η represent the curvilinear coordinates, calculated by the following formula: $\xi = (i - 1)/(i_{max} - 1)$, $\eta = (j - 1)/(j_{max} - 1)$, where i and j represent the indices in different directions of the grid, and i_{max}, j_{max} are the maximum values of the grid nodes. Due to the rich flow field information near the boundary, it is the area of greater concern throughout the simulation process. Therefore, we have designed three features: SDF , M_x , and M_y . Their calculation formulas are as follows:

$$\begin{cases} M = e^{-|SDF|}, \Psi_M(x) = M \times x, \Psi_M(y) = M \times y, \\ SDF(i, j) = \min_{(i^*, j^*) \in Z} |(i, j) - (i^*, j^*)| \text{sign}[f(i, j)] \end{cases} \quad (14)$$

SDF is used to describe the signed distance from a flow field point to the surface of the airfoil. Otherwise, the purpose of features M_x and M_y is to artificially reweight each grid point in the flow field based on the SDF parameter. Grid points closer to the airfoil surface are given greater weight, while those farther away are given smaller weight, as the numerical values of the flow field in the far field are precisely the areas we are less concerned about. As shown in Figure 5, $\frac{\partial x}{\partial \xi}$, $\frac{\partial x}{\partial \eta}$, $\frac{\partial y}{\partial \xi}$, and $\frac{\partial y}{\partial \eta}$ represent the Jacobian matrices used in the coordinate transformation. The right-hand side of Eq. (14) represents the predictions of QLingNet, which are the velocity field and pressure field. Since flow parameters often vary significantly at the leading and trailing edges of the airfoil, the gradient information of velocity $(\frac{\partial u}{\partial \xi}, \frac{\partial u}{\partial \eta}, \frac{\partial v}{\partial \xi}, \frac{\partial v}{\partial \eta})$ and pressure $(\frac{\partial p}{\partial \xi}, \frac{\partial p}{\partial \eta})$ is added as constraint terms to the loss function. The loss function used during model training is the mean squared error (MSE), calculated as:

$$\begin{aligned} MSE_{loss} = & \frac{1}{9 \times N} \sum_{i=1}^N [(u_i^t - u_i^k)^2 + (v_i^t - v_i^k)^2 + (p_i^t - p_i^k)^2 + \\ & ((\frac{\partial u}{\partial \xi})_i^t - (\frac{\partial u}{\partial \xi})_i^k)^2 + ((\frac{\partial u}{\partial \eta})_i^t - (\frac{\partial u}{\partial \eta})_i^k)^2 + ((\frac{\partial v}{\partial \xi})_i^t - (\frac{\partial v}{\partial \xi})_i^k)^2 + \\ & ((\frac{\partial v}{\partial \eta})_i^t - (\frac{\partial v}{\partial \eta})_i^k)^2 + ((\frac{\partial p}{\partial \xi})_i^t - (\frac{\partial p}{\partial \xi})_i^k)^2 + ((\frac{\partial p}{\partial \eta})_i^t - (\frac{\partial p}{\partial \eta})_i^k)^2] \end{aligned} \quad (15)$$

Here, N is the number of samples, φ_i^t and φ_i^k ($\varphi : u, v, p, \frac{\partial u}{\partial \xi}, \frac{\partial u}{\partial \eta}, \frac{\partial v}{\partial \xi}, \frac{\partial v}{\partial \eta}, \frac{\partial p}{\partial \xi}, \frac{\partial p}{\partial \eta}$) represent the ground truth and predicted values by QLingNet, respectively.

4. Results and discussions

4.1. Ablation experiments

Firstly, ablative experiments were conducted on the model to select the optimal hyperparameters. The initial learning rate during the training process was set to 5×10^{-5} . The Adam optimizer was employed to optimize the model parameters during training, with a batch size of 1. The program code was written using the Python language and the PyTorch deep learning framework. Additionally, the training of the QLingNet model was accelerated by utilizing an RTX 3090 GPU. The MSE mentioned in Section 3 was utilized as the loss function during model training. Additionally, to facilitate model convergence, a learning rate scheduler was employed to automatically adjust the learning rate during the training process. Here, the learning rate step size was set to 50, and the hyperparameter *gamma* was set to 0.1, indicating that every 50 iterations during model training, the learning rate was multiplied by 0.1. The model completed a total of 500 iterations of training.

Figure 6 and Table 1 respectively present the variation curves of the loss function during training under five different hyperparameter settings, along with detailed parameter configuration information. As indicated in the second column of Table 1, the first hyperparameter is the *stepsize* of CycleFC mentioned in Section 2.2. A larger value of this parameter implies a larger receptive field of the model. However, from the training results, a larger receptive field does not necessarily correspond to better generalization performance. From Model 1 to Model 2, with the increase in the *stepsize* value, the loss function slightly decreases. However, when this value increases from 11 to 13, although a smaller loss function is achieved on the training set, the loss function on the cross-validation set increases. Therefore, in this study, the *stepsize* is set to 11.

As shown in the third column of Table 1, the second hyperparameter is "layers", which represents the number of CycleMLP Block modules in each stage of the QLingNet network. Similarly, from the test results of Model 4 to Model 5, it can be observed that as the number of CycleMLP Blocks increases in each stage, the loss function on both the training set and the cross-validation set increases. Therefore, in this study, the layers in the encoding and decoding stages of the model are set to 2, 2, 4, 2, and 2, 4, 2, 2, respectively. As shown in the fourth column of Table 1, the third hyperparameter is "embedding dimension", which corresponds to the "layers" hyperparameter one by one.

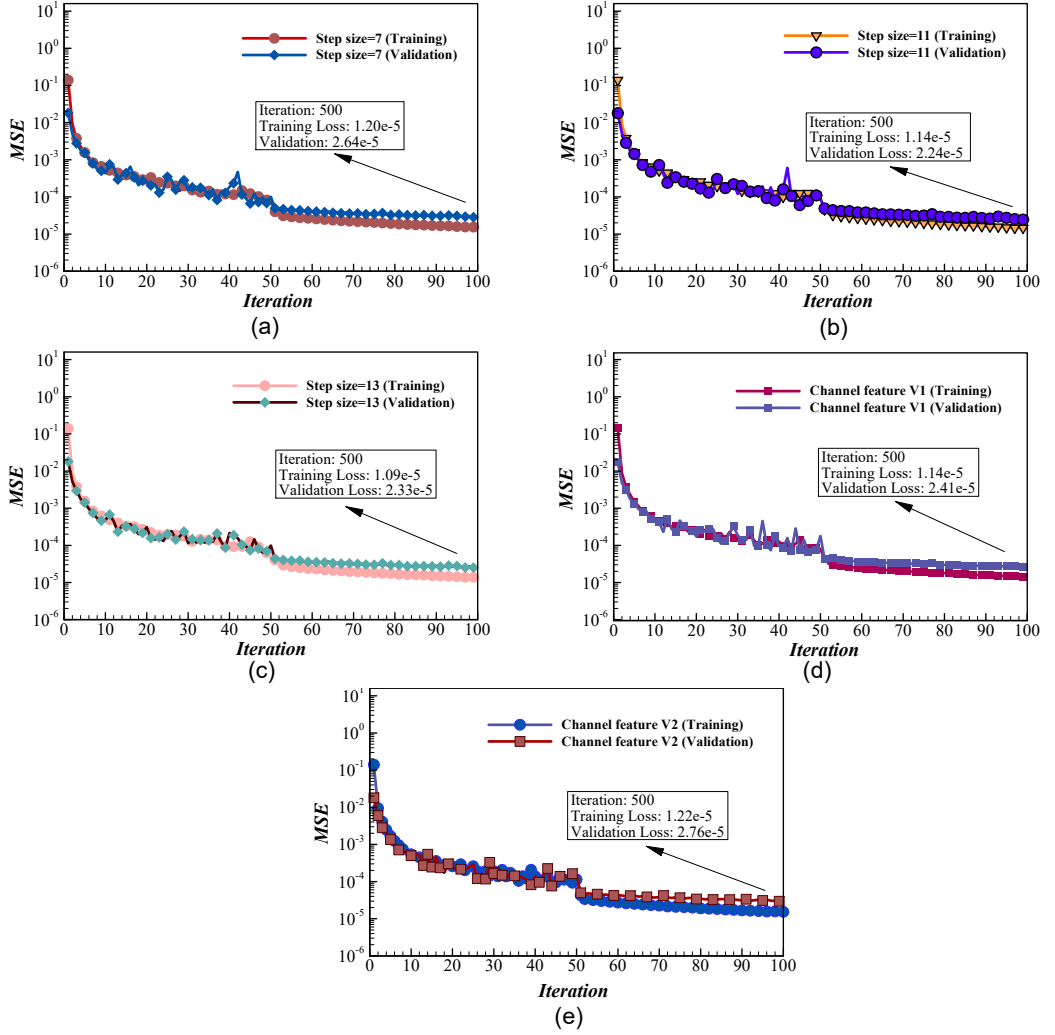


Figure 6: Loss function variation curves of QLingNet trained with different hyperparameters.

Table 1: Ablation experiment results of QLingNet

Name	Stepsize	Layers	Embedding dimension	Training loss	Validation loss
Model 1	7	[2, 2, 4, 2]	[64, 128, 320, 512]	1.20×10^{-5}	2.64×10^{-5}
		[2, 4, 2, 2]	[512, 320, 128, 64]		
Model 2	11	[2, 2, 4, 2]	[64, 128, 320, 512]	1.14×10^{-5}	2.24×10^{-5}
		[2, 4, 2, 2]	[512, 320, 128, 64]		
Model 3	13	[2, 2, 4, 2]	[64, 128, 320, 512]	1.09×10^{-5}	2.33×10^{-5}
		[2, 4, 2, 2]	[512, 320, 128, 64]		
Model 4	13	[2, 2, 4, 2]	[64, 128, 256, 512]	1.14×10^{-5}	2.41×10^{-5}
		[2, 4, 2, 2]	[512, 256, 128, 64]		
Model 5	13	[4, 4, 6, 4]	[64, 128, 256, 512]	1.22×10^{-5}	2.76×10^{-5}
		[4, 6, 4, 4]	[512, 256, 128, 64]		

It represents the size of the feature dimension in each stage during the down-sampling or up-sampling process of the model. By comparing the test results of Model 3 and Model

4, it can be observed that this parameter also affects the test results. According to the test results, in the decoding and encoding stages of the model, this value is set to 64, 128, 320, 512, and 512, 320, 128, 64, respectively. Additionally, Figure 6 presents the curves of the loss function for the five different models on both the training set and the cross-validation set. At the initial training stage, the loss function curves of all five models show a decreasing trend with an increase in the number of iterations. However, as depicted in Figure 6(b), corresponding to Model 2 in Table 1, the loss function on the cross-validation set is the smallest, indicating the best generalization performance of the model under the current parameters. Based on the above analysis, the parameters of Model 2 are selected as the hyperparameters for QLingNet during the model training process.

4.2. Analysis of flow field prediction results

4.2.1. Analysis of NACA0012-CST dataset test results

We evaluate the flow field prediction performance of the QLingNet model using airfoils that were not included in the training dataset, as described in Section 3. The initial testing focuses on the NACA0012-CST airfoil database, where 500 airfoils are encoded as NACA0012-CST i ($i = 1, 2, \dots, 500$). We specifically select the NACA0012-CST15 airfoil from the test set to evaluate the flow field prediction accuracy of the QLingNet model. From Figure 7, it can be observed that there is good consistency between the CFD calculated results and QLingNet predictions. Furthermore, the absolute error plots in Figure 7 reveal that for velocity u , the error values range from 5×10^{-3} to 5.5×10^{-2} ; for velocity v , the absolute error values range from 5×10^{-3} to 7×10^{-2} ; and for pressure p , the absolute error values range from 5×10^{-3} to 5×10^{-2} . Otherwise, by examining the absolute error histograms in Figure 8, it is evident that the majority of errors for velocity u , v , and pressure p are less than 1×10^{-2} . This indicates that the proposed QLingNet neural network model achieves a satisfactory prediction performance.

To further test the accuracy of QLingNet's flow field prediction results, Figure 9 provides contour plots comparing CFD with QLingNet, histograms of data distribution, and corresponding kernel density plots. From the test results in Figure 9, the contour plots between CFD and QLingNet generally exhibit good fitting. However, there are certain areas where the fitting effect for velocity u is less ideal. This observation is also evident from the histograms of data distribution, where the majority of the data distribution shows good fitting, with noticeable differences only in the vicinity of the value 1.

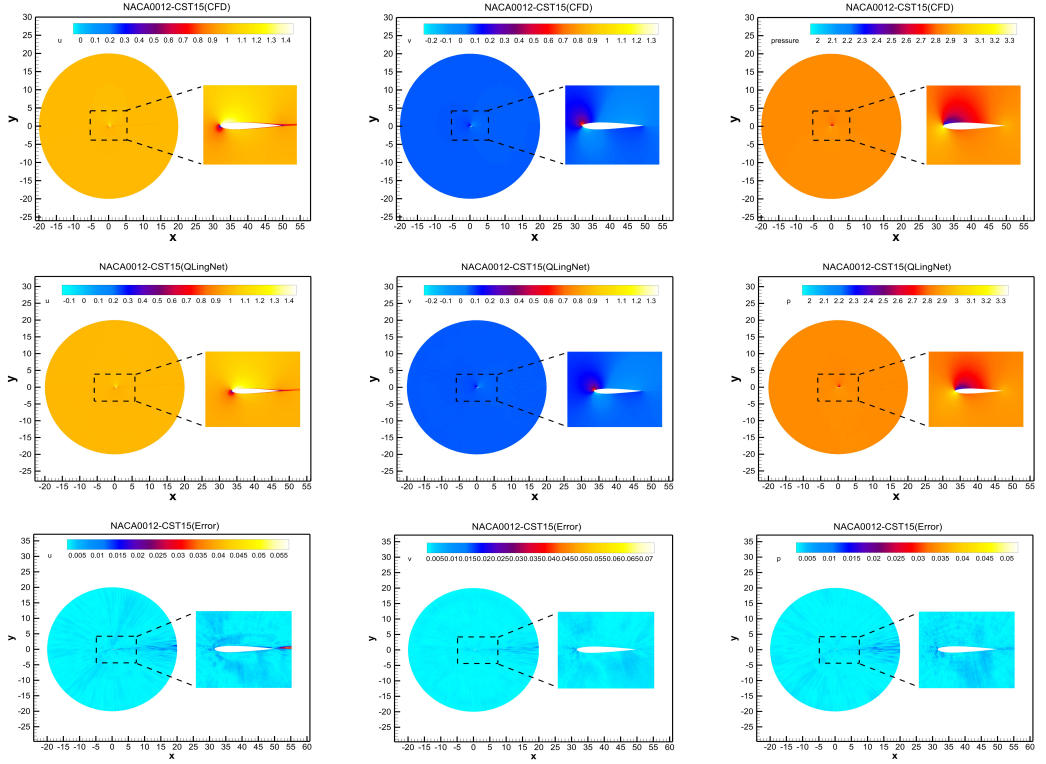


Figure 7: Visualization comparing the CFD-calculated and neural network-predicted values of velocity (u , v) and pressure (p) for the NACA0012-CST15 airfoil, alongside corresponding absolute error plots.

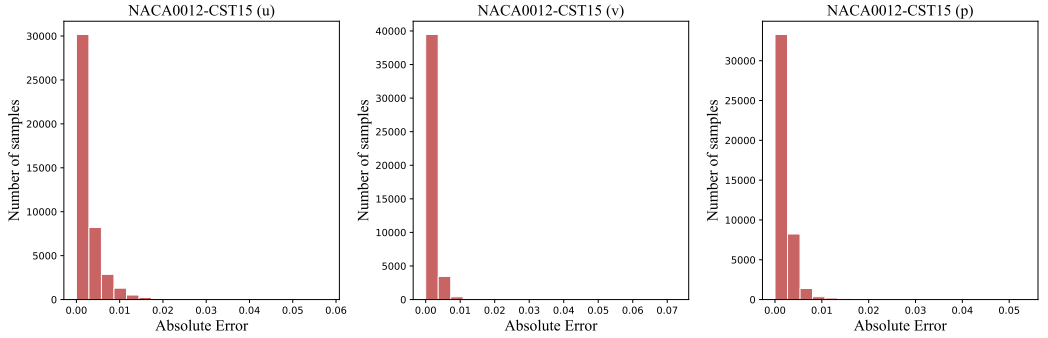


Figure 8: Histogram of the absolute error distribution between CFD and Q LingNet.

Nonetheless, further examination of the kernel density plots reveals minimal impact on the density plots due to subtle differences in the data. The higher peaks in the kernel density plot indicate denser data at those locations, which is consistent with the display results of the data distribution histogram. Overall, the test results fully meet the engineering requirements. For velocity v and pressure p , the fitting between CFD and Q LingNet is relatively good in both contour plots and histograms of data distribution. This indicates that as a black-box model, Q LingNet is capable of training based on historical data to

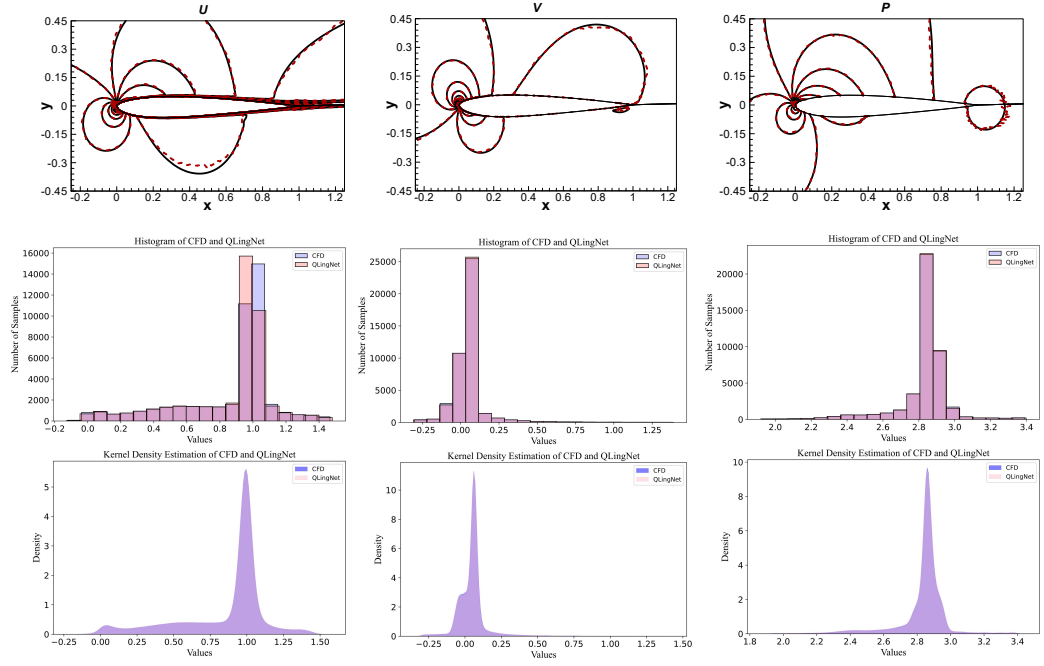


Figure 9: First row: Contour plots between Q LingNet flow field predictions and CFD computational results. The solid black line represents the CFD calculation values, while the dashed red line represents the Q LingNet prediction results. Second row: Histogram comparing the data distribution between CFD and Q LingNet. Third row: Kernel density plot comparing Q LingNet and CFD.

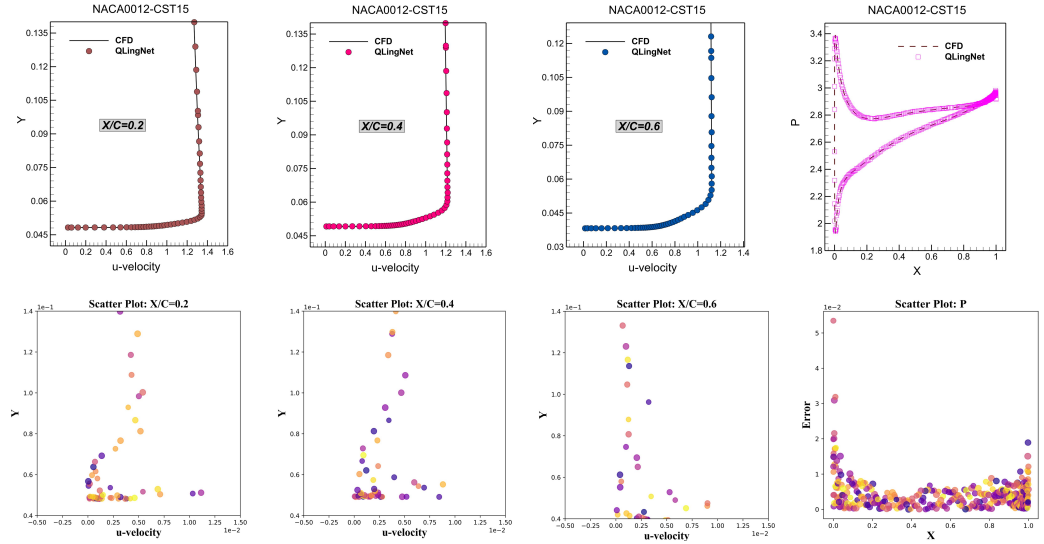


Figure 10: First row: Velocity fitting curves and near-wall pressure fitting curves of CFD and Q LingNet at different station points. Second row: Scatter plots of velocity absolute errors at different station points and near-wall pressure absolute error scatter plots between CFD and Q LingNet.

predict the flow field of new airfoils with different data distributions, achieving excellent predictive performance.

Figure 10 depicts the velocity profile fitting curves between Q LingNet and CFD at

three different station points, as well as the pressure profile fitting curves at the airfoil surface, along with scatter plots of the absolute errors corresponding to each curve. In Figure 10, the first three columns depict the velocity fitting curves of velocity u at positions 0.2, 0.4, and 0.6 on the airfoil boundary, respectively, comparing CFD with QLingNet. The test results demonstrate that at these three positions, both the CFD calculated results and the QLingNet predicted curves fit well. Furthermore, from the corresponding scatter plots of absolute errors, it is observed that at position 0.2, most absolute error values are below 5×10^{-3} with a maximum error of 1.25×10^{-2} , while at positions 0.4 and 0.6, the majority of absolute error values are below 7.5×10^{-3} , with only a few outliers ranging from 7.5×10^{-3} to 1×10^{-2} . Additionally, the last column of Figure 10 illustrates the good fitting effect of pressure curves between QLingNet predictions and CFD calculations, with the majority of absolute error values being less than 1×10^{-2} . From the above test results, QLingNet achieved good predictive performance when facing the NACA0012-CST test data. Additionally, to comprehensively test the model’s generalization capability, Appendix A provides the prediction results of more test cases.

4.2.2. Analysis of test results for the UIUC dataset

To assess the predictive accuracy and generalization capability of QLingNet across flow fields of different resolutions, Figure 11 presents the flow field prediction results for the ah81k144 airfoil from the UIUC airfoil database. Figure 11 illustrates that the flow field predictions of QLingNet exhibit a high degree of similarity with the results of CFD calculations. Furthermore, from the contour plots of absolute errors between the predicted values of QLingNet and the CFD computed values, it can be observed that for the velocity component u , the absolute error ranges from 5×10^{-3} to 6×10^{-2} , for the velocity component v , the absolute error ranges from 5×10^{-3} to 5×10^{-2} , and for the pressure p , the absolute error ranges from 5×10^{-3} to 4.5×10^{-2} . Furthermore, from the histogram in Figure 12 depicting the distribution of absolute errors between CFD and QLingNet, it is evident that for both velocity components u and v , as well as pressure p , the majority of error values are centered around zero. Overall, the numerical range of errors lies between 0 and 2×10^{-2} , indicating a high level of predictive accuracy.

For a more detailed assessment of QLingNet’s predictive accuracy, Figure 13 provides contour plots comparing predicted values to ground truth, histograms illustrating the distribution of flow field data, and corresponding kernel density plots. From the first

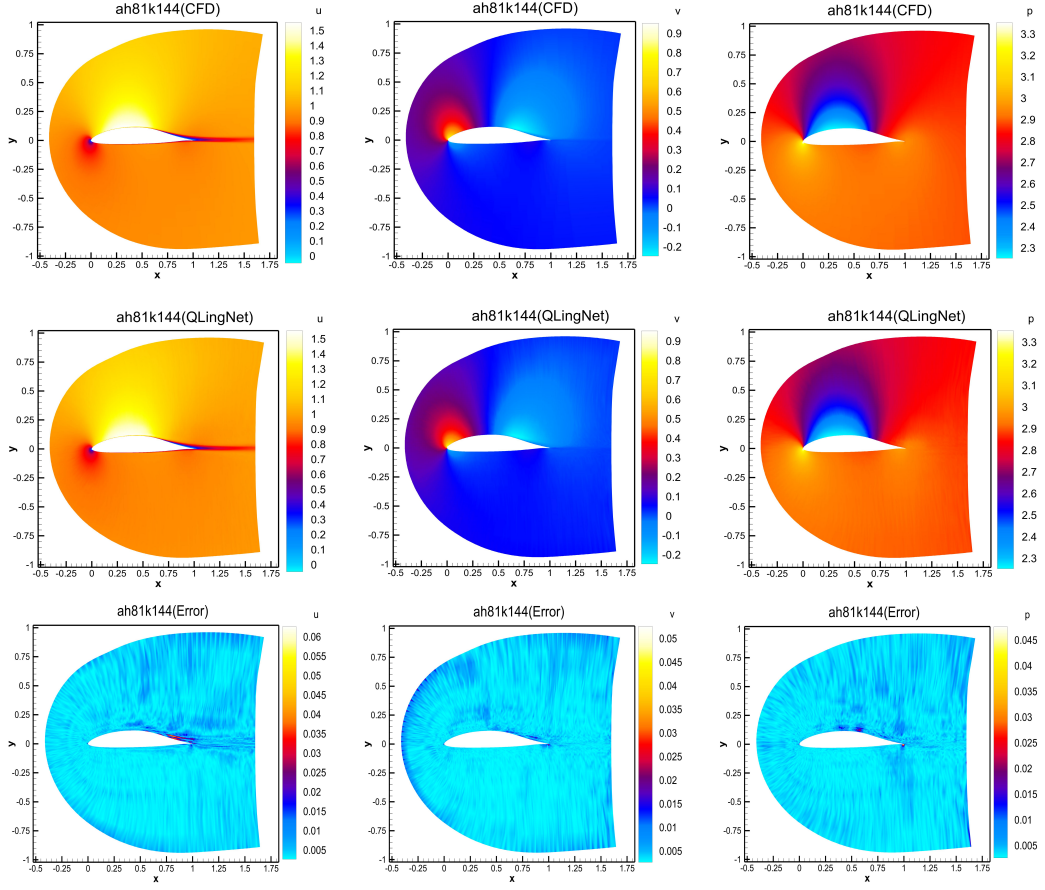


Figure 11: Comparison between the CFD computational results and the predicted results of the Q LingNet for ah81k144, alongside corresponding absolute error plots.

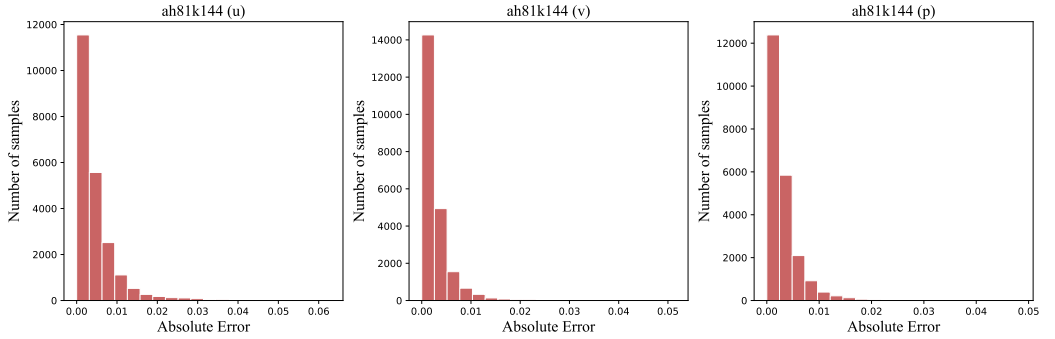


Figure 12: Histogram of the absolute error distribution between CFD and Q LingNet.

row of Figure 13, it's evident that the lines between CFD and Q LingNet fit perfectly. Additionally, the histograms in the second row show that, except for some differences in the histogram of pressure data, the distribution histograms of CFD computed data and Q LingNet predicted data generally match well. Any differences in data distribution occur in adjacent regions, indicating close proximity of data in those locations. Furthermore,

examining the kernel density plots in the third row reveals that the data distribution is dense around peaks of the curves, indicating similar trends in data distribution. Overall, even when facing flow fields of different resolutions, QLingNet demonstrates strong predictive capabilities.

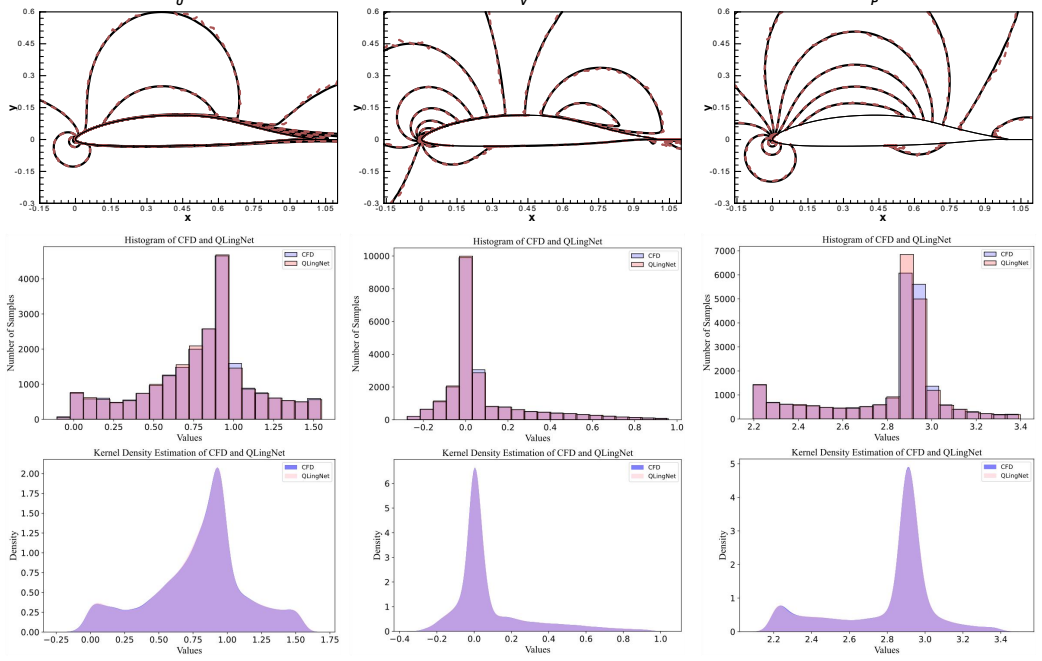


Figure 13: First row: Contour plots between QLingNet flow field predictions and CFD computational results. The solid black line represents the CFD calculation values, while the dashed red line represents the QLingNet prediction results. Second row: Histogram comparing the data distribution between CFD and QLingNet. Third row: Kernel density plot comparing QLingNet and CFD..

The above analyses have focused on QLingNet's predictive accuracy at the macroscopic scale of the flow field. Figure 14 provides fitting curves of velocity u at three different stations on the airfoil near-wall, as well as fitting curves of pressure distribution on the surface. It can be observed that at stations 0.2, 0.4, and 0.6, the curves of CFD and QLingNet fit well, and similarly, for the pressure curve p , a good fitting effect is also achieved. In the second row of Figure 14, scatter plots of absolute errors corresponding to each fitting curve are provided. For the velocity u at station 0.2, the error data are mostly within the numerical range of 5×10^{-3} , with only some error points falling between 5×10^{-3} and 1×10^{-2} . At station 0.4, the error data are primarily within the range of 0 to 1.5×10^{-2} . Similarly, at station 0.6, the error data also fall within the range of 0 to 1.5×10^{-2} . Regarding the error in pressure distribution on the surface, the majority of error data points are less than 2×10^{-2} , with only a few error data points falling between

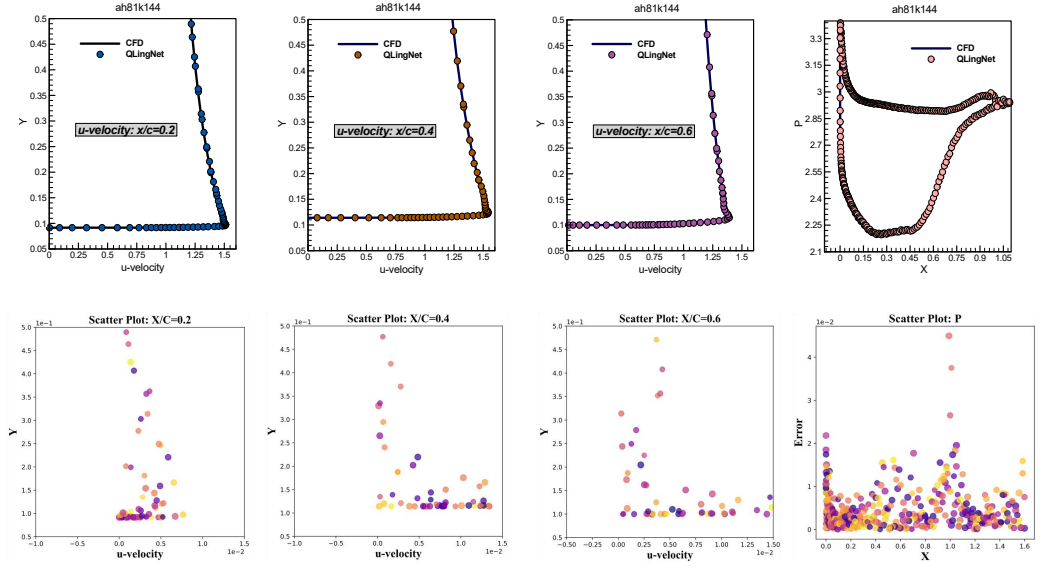


Figure 14: First row: Velocity fitting curves and near-wall pressure fitting curves of CFD and Q LingNet at different station points. Second row: Scatter plots of velocity absolute errors at different station points and near-wall pressure absolute error scatter plots between CFD and Q LingNet.

Table 2: Comparison of computation time between CFD and Q LingNet

Airfoil	CFD	Q LingNet	acceleration ratio
ah81k144	3720.28s	0.91s	4.09×10^3
e174	2433.79s	1.15s	2.12×10^3
e421	7371.24s	2.89s	2.55×10^3
eh009	2591.42s	0.93s	2.79×10^3
s8055	3727.41s	0.97s	3.84×10^3

2×10^{-2} and 4×10^{-2} . Table 2 provides comparisons between CFD computation time and Q LingNet prediction time for more test airfoils. It is evident that Q LingNet prediction speed improves by three orders of magnitude compared to CFD simulation time.

Overall, Q LingNet model demonstrates good predictive accuracy when facing UIUC airfoil flow field data with varying topological structures and resolutions. In order to comprehensively evaluate the generalization capability of the Q LingNet model, Appendix B provides additional test results concerning UIUC airfoil flow fields. Moreover, in Appendix C, further predictions of velocity and pressure curves for both NACA0012-CST airfoil flow field dataset and UIUC airfoil flow field dataset by the Q LingNet model are presented.

5. Conclusions

In this work, we propose QLingNet, which has linear computational complexity and can be used for predicting flow fields of any resolution. The CycleFC method effectively overcomes the sensitivity of traditional convolutional neural networks to flow field resolution by integrating multi-scale flow field features at the channel dimension. Additionally, a memory pool module is designed to store flow field resolution data from the down-sampling stage in a memory pool, ensuring accurate prediction and restoration of flow field data at different scales in the up-sampling stage. The model’s feature pyramid structure also ensures its adaptability to multi-scale flow field features. The test results demonstrate that QLingNet is three orders of magnitude faster than CPU-based solvers.

We provide two types of subsonic flow field datasets, NACA0012-CST and UIUC, with different geometric shapes, to test the prediction accuracy and generalization capability of the QLingNet model. The test results indicate that the QLingNet model achieves high fitting accuracy with the velocity and pressure fields compared to CFD calculation results, even when facing flow field data with different shapes and resolutions. For both velocity u , v and pressure p , the prediction accuracy exceeds 99%. The experiment also demonstrates that a larger amount of data significantly improves the modeling accuracy. In the NACA0012-CST dataset, which has more training data, the mean squared error between predicted and ground truth is on the order of $1e-6$, while in the UIUC dataset with fewer training data, the mean squared error remains at the order of $1e-5$.

Overall, the QLingNet provide strong support for engineering applications. In future work, we will explore how artificial intelligence techniques can be applied to simulate more complex flows rapidly, accelerate research on large-scale deep learning aerodynamics models, and expedite the industrial application of this technology.

The name of ‘QLingNet’

The inspiration for QLingNet comes from the Qinling Mountains. The Qinling are a major east-west mountain range in southern Shaanxi Province, China. The mountains mark the divide between the drainage basins of the Yangtze and Yellow River systems, providing a natural boundary between North and South China (see <https://en.wikipedia.org/wiki/Qinling>).

CRedit authorship contribution statement

Kuijun Zuo : Data curation, Formal analysis, Investigation, Methodology, Software, Validation, Visualization, Writing-original draft, Writing-review & editing.

Zhengyin Ye : Funding acquisition, Supervision, Resources, Project administration.

Linyang Zhu : Funding acquisition, Resources, Supervision.

Xianxu Yuan : Funding acquisition, Resources, Supervision.

Weiwei Zhang : Conceptualization, Methodology, Project administration, Supervision, Writing-review & editing.

Acknowledgments

This work was supported by the National Natural Science Foundation of China (Grant No. 12202470).

Data availability

The data and code that support the findings of this study are available by contacting the corresponding author via email.

Declaration of competing interest

The authors declare that they have no known competing financial interests or personal relationships that could have appeared to influence the work reported in this paper.

References

- [1] L. Cutrone, A. Schettino, J. I. Cardesa, G. Delattre, J. G. Coder, S. Qiang, M. M. Choudhari, E. Vogel, Transition prediction in hypersonic regime on complex geometries with rans-based models, in: AIAA SCITECH 2024 Forum, 2024, p. 0291.
- [2] J. Chaiyanupong, C. Khajorntraidet, Design and analysis of double element airfoil using rans, Journal of Research and Applications in Mechanical Engineering 12 (1) (2024).

- [3] O. Simsek, H. Islek, 2d and 3d numerical simulations of dam-break flow problem with rans, des, and les, *Ocean Engineering* 276 (2023) 114298.
- [4] V. Esfahanian, M. J. Izadi, H. Bashi, M. Ansari, A. Tavakoli, M. Kordi, Aerodynamic shape optimization of gas turbines: a deep learning surrogate model approach, *Structural and Multidisciplinary Optimization* 67 (1) (2024) 2.
- [5] E. Salimipour, On the moving surface impact on flow field and aerodynamic performance of a thick airfoil, *Ocean Engineering* 291 (2024) 116504.
- [6] J. W. Hairun Xie, M. Zhang, Knowledge-embedded meta-learning model for lift coefficient prediction of airfoils, *Expert Systems with Applications* 233 (2023) 121002.
- [7] J. Zhong, F. Qu, D. Sun, J. Tian, T. Wang, J. Bai, Fast flow field prediction approach of supersonic inlet in wide operating range based on deep learning, *Aerospace Science and Technology* (2024) 108955.
- [8] K. Shukla, V. Oommen, A. Peyvan, M. Penwarden, N. Plewacki, L. Bravo, A. Ghoshal, R. M. Kirby, G. E. Karniadakis, Deep neural operators as accurate surrogates for shape optimization, *Engineering Applications of Artificial Intelligence* 129 (2024) 107615.
- [9] S. Yetkin, S. Abuhanieh, S. Yigit, Investigation on the abilities of different artificial intelligence methods to predict the aerodynamic coefficients, *Expert Systems with Applications* 237 (2024) 121324.
- [10] Y. Wang, R. Dan, S. Luo, L. Sun, Q. Wu, Y. Li, X. Chen, K. Yan, X. Ye, D. Yu, Amsc-net: Anatomy and multi-label semantic consistency network for semi-supervised fluid segmentation in retinal oct, *Expert Systems with Applications* (2024) 123496.
- [11] D. Soler, O. Mariño, D. Huergo, M. de Frutos, E. Ferrer, Reinforcement learning to maximize wind turbine energy generation, *Expert Systems with Applications* 249 (2024) 123502.
- [12] A. M. Ismael, A. Şengür, Deep learning approaches for covid-19 detection based on chest x-ray images, *Expert Systems with Applications* 164 (2021) 114054.
- [13] S. Zhu, S. Li, D. Xiong, Vistfc: Vision-guided target-side future context learning for neural machine translation, *Expert Systems with Applications* (2024) 123411.

- [14] X. Guo, W. Li, F. Iorio, Convolutional neural networks for steady flow approximation, in: Proceedings of the 22nd ACM SIGKDD international conference on knowledge discovery and data mining, 2016, pp. 481–490.
- [15] M.-Y. Wu, Y. Wu, X.-Y. Yuan, Z.-H. Chen, W.-T. Wu, N. Aubry, Fast prediction of flow field around airfoils based on deep convolutional neural network, *Applied Sciences* 12 (23) (2022) 12075.
- [16] M. D. Ribeiro, A. Rehman, S. Ahmed, A. Dengel, Deepcfd: Efficient steady-state laminar flow approximation with deep convolutional neural networks, *arXiv preprint arXiv:2004.08826* (2020).
- [17] J.-W. Hu, W.-W. Zhang, Mesh-conv: Convolution operator with mesh resolution independence for flow field modeling, *Journal of Computational Physics* 452 (2022) 110896.
- [18] C. Duru, H. Alemdar, Ö. U. Baran, Cnnfoil: Convolutional encoder decoder modeling for pressure fields around airfoils, *Neural Computing and Applications* 33 (12) (2021) 6835–6849.
- [19] C. Duru, H. Alemdar, O. U. Baran, A deep learning approach for the transonic flow field predictions around airfoils, *Computers & Fluids* 236 (2022) 105312.
- [20] D. Sun, Z. Wang, F. Qu, J. Bai, A deep learning based prediction approach for the supercritical airfoil at transonic speeds, *Physics of Fluids* 33 (8) (2021).
- [21] M. Leer, A. Kempf, Fast flow field estimation for various applications with a universally applicable machine learning concept, *Flow, Turbulence and Combustion* 107 (2021) 175–200.
- [22] W. Haizhou, L. Xuejun, A. Wei, L. Hongqiang, A generative deep learning framework for airfoil flow field prediction with sparse data, *Chinese Journal of Aeronautics* 35 (1) (2022) 470–484.
- [23] H. Wu, X. Liu, W. An, S. Chen, H. Lyu, A deep learning approach for efficiently and accurately evaluating the flow field of supercritical airfoils, *Computers & Fluids* 198 (2020) 104393.

- [24] Z. Wang, X. Liu, J. Yu, H. Wu, H. Lyu, A general deep transfer learning framework for predicting the flow field of airfoils with small data, *Computers & Fluids* 251 (2023) 105738.
- [25] Z. Yang, Y. Dong, X. Deng, L. Zhang, Amgnet: Multi-scale graph neural networks for flow field prediction, *Connection Science* 34 (1) (2022) 2500–2519.
- [26] F. Ogoke, K. Meidani, A. Hashemi, A. B. Farimani, Graph convolutional networks applied to unstructured flow field data, *Machine Learning: Science and Technology* 2 (4) (2021) 045020.
- [27] J. Li, T. Liu, Y. Wang, Y. Xie, Integrated graph deep learning framework for flow field reconstruction and performance prediction of turbomachinery, *Energy* 254 (2022) 124440.
- [28] G. Chen, M. Wang, Y. Yang, K. Yu, L. Yuan, Y. Yue, Pointgpt: Auto-regressively generative pre-training from point clouds, *Advances in Neural Information Processing Systems* 36 (2024).
- [29] A. Abbas, A. Rafiee, M. Haase, A. Malcolm, Geometrical deep learning for performance prediction of high-speed craft, *Ocean Engineering* 258 (2022) 111716.
- [30] J. Jiang, G. Li, Y. Jiang, L. Zhang, X. Deng, Transcfd: A transformer-based decoder for flow field prediction, *Engineering Applications of Artificial Intelligence* 123 (2023) 106340.
- [31] A. Hemmasian, A. Barati Farimani, Reduced-order modeling of fluid flows with transformers, *Physics of Fluids* 35 (5) (2023).
- [32] Z. Deng, J. Wang, H. Liu, H. Xie, B. Li, M. Zhang, T. Jia, Y. Zhang, Z. Wang, B. Dong, Prediction of transonic flow over supercritical airfoils using geometric-encoding and deep-learning strategies, *arXiv preprint arXiv:2303.03695* (2023).
- [33] K. Zuo, Z. Ye, W. Zhang, X. Yuan, L. Zhu, Fast aerodynamics prediction of laminar airfoils based on deep attention network, *Physics of Fluids* 35 (3) (2023).
- [34] S. Chen, E. Xie, C. Ge, R. Chen, D. Liang, P. Luo, Cyclemlp: A mlp-like architecture for dense prediction. *arxiv* 2021, *arXiv preprint arXiv:2107.10224*.

- [35] K. Swannet, C. Varriale, A. K. Doan, Towards universal parameterization: Using variational autoencoders to parameterize airfoils, in: AIAA SCITECH 2024 Forum, 2024, p. 0686.
- [36] K. Lane, D. Marshall, Inverse airfoil design utilizing cst parameterization, in: 48th AIAA Aerospace Sciences Meeting Including the New Horizons Forum and Aerospace Exposition, 2010, p. 1228.
- [37] Z. Zhao, L. He, X.-y. HE, Design of general cfd software phenglei, Computer Engineering & Science 42 (02) (2020) 210.
- [38] K. Zuo, Z. Ye, S. Bu, X. Yuan, W. Zhang, Fast simulation of airfoil flow field via deep neural network, arXiv preprint arXiv:2312.04289 (2023).

Appendix A. NACA0012-CST dataset test results

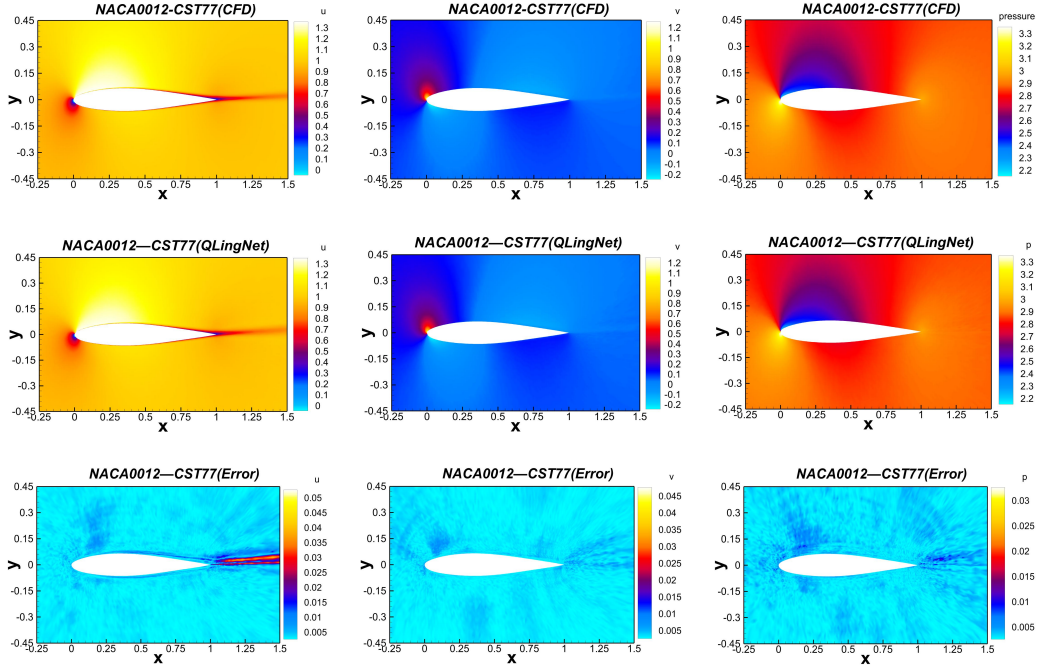


Figure A.1: NACA0012-CST77 airfoil flow field CFD calculation results, Q LingNet prediction results, and corresponding absolute error plot.

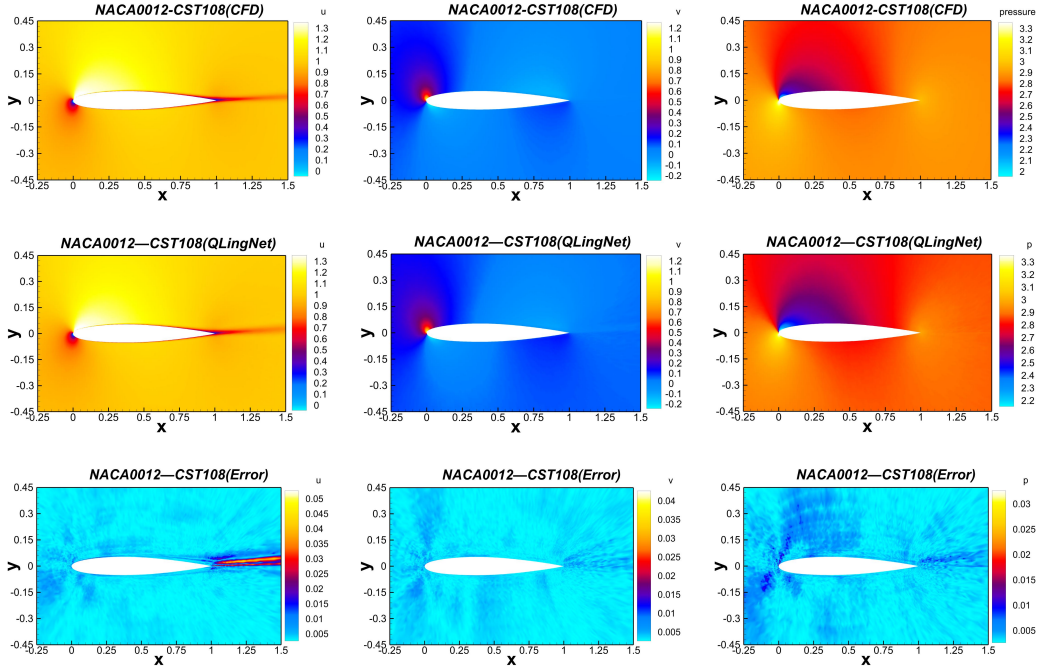


Figure A.2: NACA0012-CST108 airfoil flow field CFD calculation results, Q LingNet prediction results, and corresponding absolute error plot.

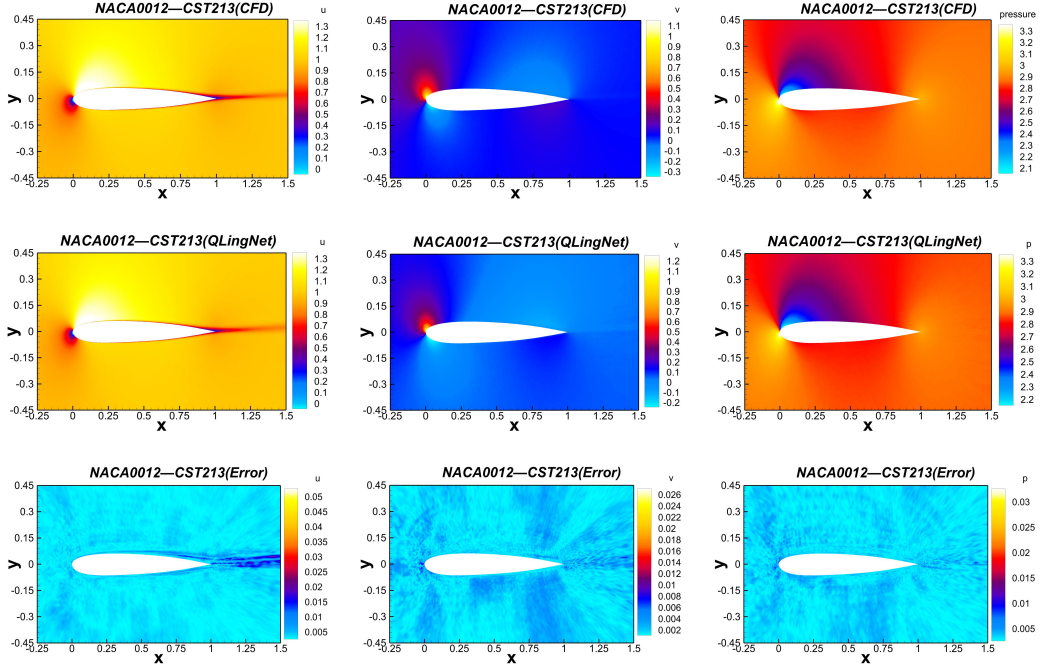


Figure A.3: NACA0012-CST213 airfoil flow field CFD calculation results, Q LingNet prediction results, and corresponding absolute error plot.

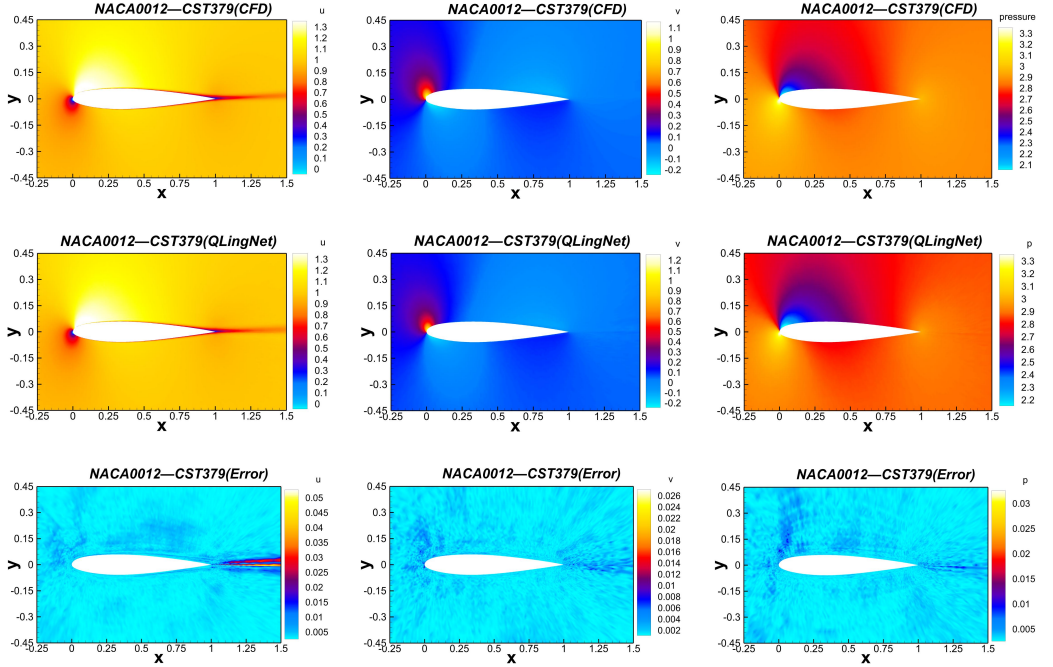


Figure A.4: NACA0012-CST379 airfoil flow field CFD calculation results, Q LingNet prediction results, and corresponding absolute error plot.

Appendix B. UIUC dataset test results

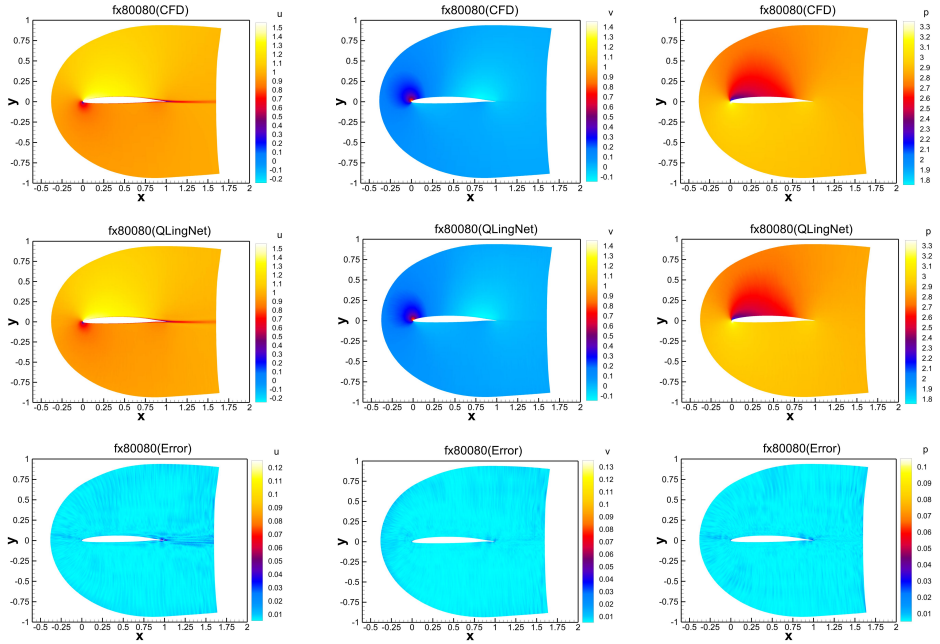


Figure B.1: fx80080 airfoil flow field CFD calculation results, QLingNet prediction results, and corresponding absolute error plot.

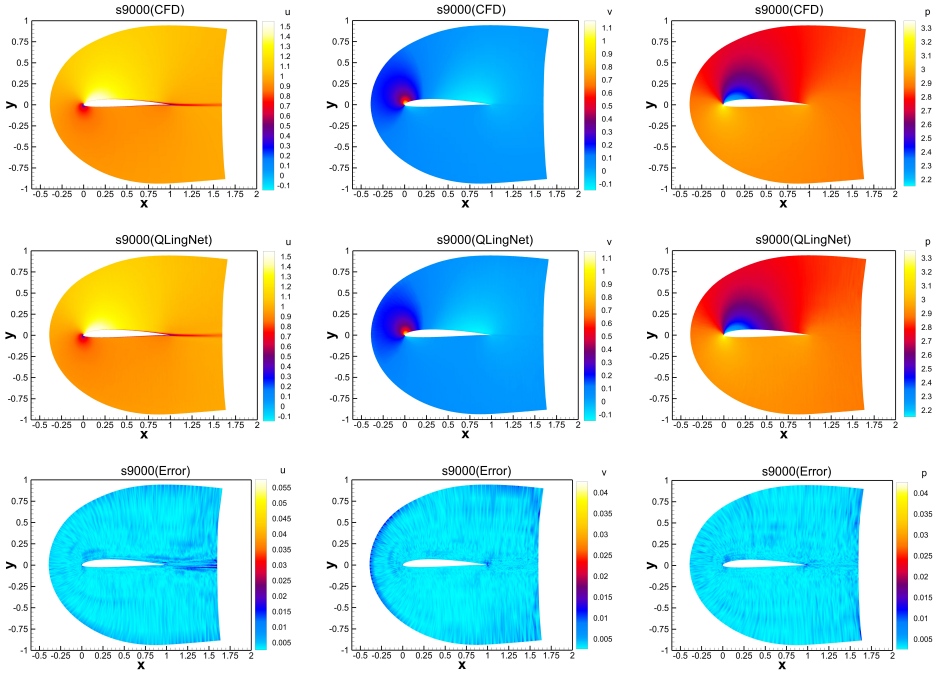


Figure B.2: s9000 airfoil flow field CFD calculation results, QLingNet prediction results, and corresponding absolute error plot.

Appendix C. Fitting curves for velocity and pressure

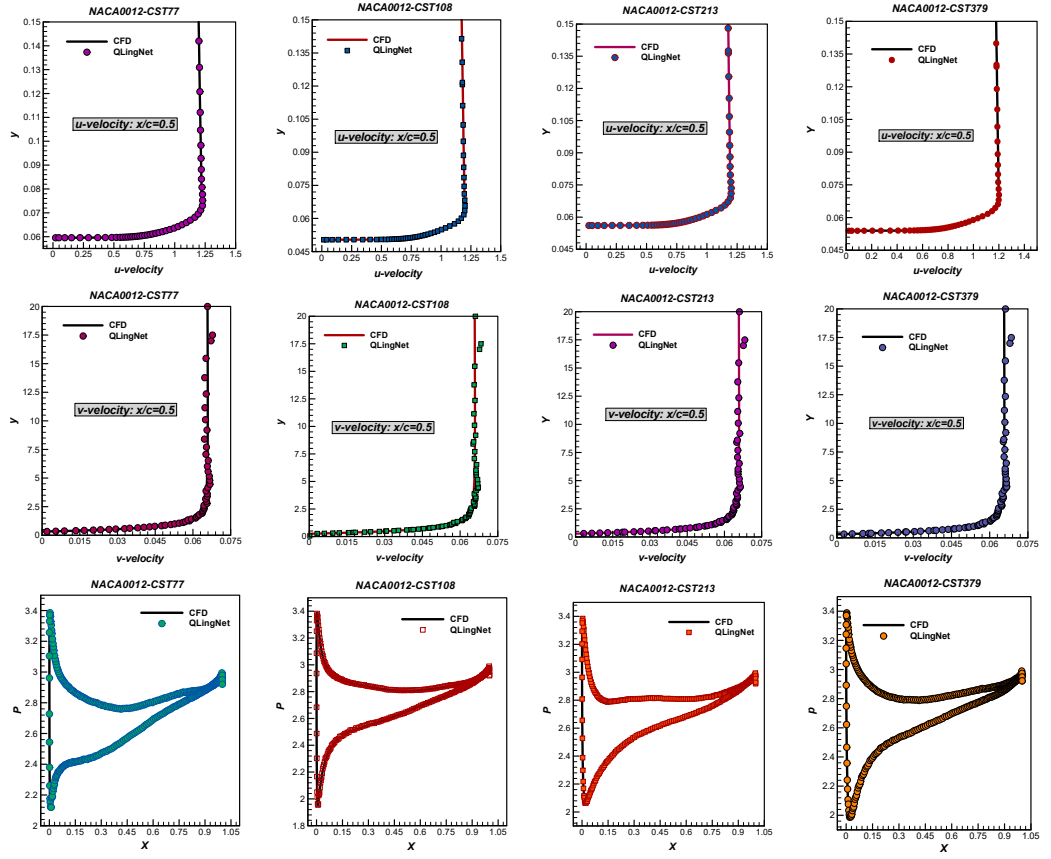


Figure C.1: Velocity and pressure fitting curves for four different test cases in the NACA0012-CST dataset.

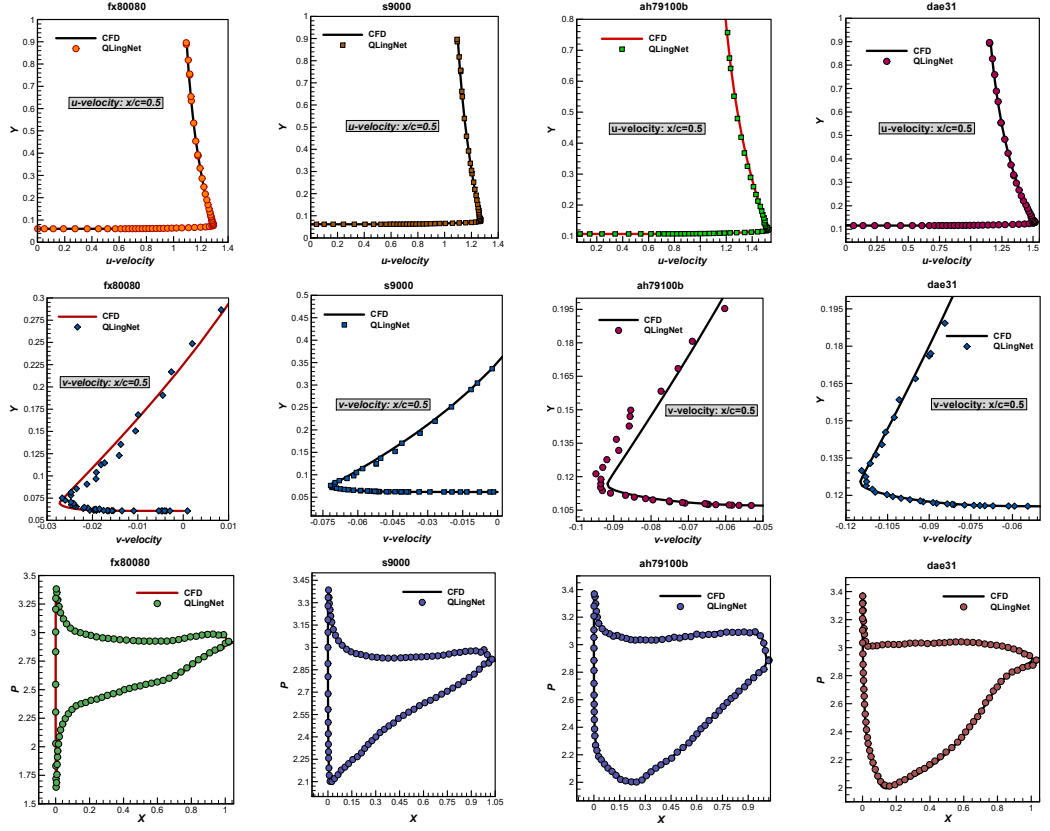


Figure C.2: Velocity and pressure fitting curves for four different test cases in the UIUC dataset.

Table C.1: Error analysis for various test cases

Airfoil	$U_{\varrho,\varsigma}$	$V_{\varrho,\varsigma}$	$P_{\varrho,\varsigma}$	$P_{\varrho,F}$	$P_{\delta,F}$	$P_{\epsilon,F}$
NACA0012-CST77	0.358%	2.775%	0.120%	0.057%	5.496×10^{-6}	1.606×10^{-3}
NACA0012-CST108	0.443%	8.640%	0.158%	0.066%	7.443×10^{-6}	1.842×10^{-3}
NACA0012-CST213	0.326%	3.369%	0.118%	0.059%	5.415×10^{-6}	1.655×10^{-3}
NACA0012-CST379	0.275%	2.588%	0.095%	0.048%	3.948×10^{-6}	1.345×10^{-3}
fx80080	0.508%	13.243%	0.281%	0.156%	6.639×10^{-5}	4.011×10^{-3}
s9000	0.450%	4.611%	0.180%	0.108%	1.741×10^{-5}	2.921×10^{-3}
ah79100b	0.778%	10.648%	0.316%	0.184%	4.646×10^{-5}	5×10^{-3}
dae31	0.657%	9.293%	0.376%	0.222%	7.517×10^{-5}	5.808×10^{-3}

Use Mean Squared Error (MSE), Mean Absolute Error (MAE), and Mean Absolute Percentage Error (MAPE) to evaluate the prediction accuracy of the velocity and pressure curves in Figure C.1 and Figure C.2, as well as the prediction accuracy of the global pressure field. MSE represents the average squared difference between the predicted values and the true values for all samples. Its calculation formula is as follows:

$$\text{MSE} = \frac{1}{n} \sum_{i=1}^n (x_i - \hat{x}_i)^2 \quad (\text{C.1})$$

Where n denotes the number of samples, x_i represents the ground truth of the i -th sample, and \hat{x}_i represents the predicted value of the i -th sample. MAE represents the average absolute difference between the predicted values and the true values for all samples. Its calculation formula is as follows:

$$\text{MAE} = \frac{1}{n} \sum_{i=1}^n |y_i - \hat{y}_i| \quad (\text{C.2})$$

The MAPE represents the average absolute value of the ratio of the prediction error to the true value for all samples, expressed as a percentage. Its calculation formula is as follows:

$$\text{MAPE} = \frac{1}{n} \sum_{i=1}^n \left| \frac{z_i - \hat{z}_i}{z_i} \right| \times 100\% \quad (\text{C.3})$$

In Table C.1, MSE, MAE, and MAPE are denoted by symbols δ , ϵ and ϱ , respectively. F represents the error of the whole-domain pressure field, and ς represents the error of the curve in Figure C.1 and C.2. For example, $U_{\delta,\varsigma}$ represents the Mean Squared Error of the velocity curve u . $P_{\varrho,F}$ represents the MAPE of the whole-domain pressure field.